UNIVERSITY OF LEEDS

Article:
Isoniemi, T, Maccaferri, N, Ramasse, QM orcid.org/0000-0001-7466-2283 et al. (2 more authors) (2020) Electron Energy Loss Spectroscopy of Bright and Dark Modes in Hyperbolic Metamaterial Nanostructures. Advanced Optical Materials, 8 (13). 2000277. ISSN 2195-1071

https://doi.org/10.1002/adom.202000277

Electron Energy Loss Spectroscopy of Bright and Dark Modes in Hyperbolic Metamaterial Nanostructures

*Tommi Isoniemi, Nicolò Maccaferri, Quentin M. Ramasse, Giuseppe Strangi, and Francesco De Angelis**

Dr. T. Isoniemi, Dr. N. Maccaferri, Dr. F. De Angelis
Istituto Italiano di Tecnologia, Via Morego 30, 16163 Genova, Italy
E-mail: francesco.deangelis@iit.it
Dr. T. Isoniemi
Current address: Department of Physics and Astronomy, University of Sheffield, Sheffield, S3 7RH, UK
Dr. N. Maccaferri
Department of Physics and Materials Science, University of Luxembourg, 162a avenue de la Faïencerie, L-1511 Luxembourg, Luxembourg
Prof. Q. M. Ramasse
SuperSTEM Laboratory, SciTech Daresbury Campus, Keckwick Lane, Daresbury, WA4 4AD, UK
School of Physics and School of Chemical and Process Engineering, University of Leeds, Leeds, LS2 9JT, UK
Prof. Giuseppe Strangi
Department of Physics, Case Western Reserve University, 10600 Euclid Avenue, Cleveland, Ohio 44106, USA
CNR-NANOTEC Istituto di Nanotecnologia and Department of Physics, University of Calabria, 87036, Italy

Keywords: hyperbolic metamaterials, EELS, nanoparticles, plasmons, STEM

Layered metal/dielectric hyperbolic metamaterials (HMMs) support a wide landscape of plasmon polariton excitations. In addition to surface plasmon polaritons, coupled Bloch-like gap-plasmon polaritons with high modal confinement inside the multilayer are supported. Photons can excite only a subset of these polaritonic modes, typically with a limited energy and momentum range in respect to the wide set of high-K modes supported by hyperbolic dispersion media, and coupling with gratings or local excitation is necessary. Strikingly, electron energy loss spectroscopy (EELS) in a scanning transmission electron microscope allows nm-scale local excitation and mapping of the spatial field distribution of all the modes supported by a photonic or plasmonic structure, both bright and dark, and also all other inelastic interactions of the beam, including phonons and interband transitions. Herein, experimental evidence of the spatial distribution of plasmon polaritons in multilayered type II

HMM nanostructures is acquired with an aloof electron beam adjacent to structures of current interest. HMM pillars are useful for their separation and adjustability of optical scattering and absorption, while HMM slot cavities can be used as waveguides with high field confinement. The nature of the modes is confirmed with corresponding simulations of EEL and optical spectra and near-field intensities.

1. Introduction

Optical metamaterials are composed of sub-wavelength structures and exhibit unusual electromagnetic properties not observed in nature.[1] One class of these materials, hyperbolic metamaterials (HMMs), are highly anisotropic media with opposite signs of permittivity tensor components in different directions. As such, the motion of free electrons is confined to one (type I) or two (type II) spatial dimensions, and the dispersion relation of HMMs is hyperbolic.[2] These materials can be engineered to have unusual properties, including broadband perfect absorption using particles[3] or gratings,[4] negative refraction[5], and resonant gain singularities.[6] There is a wide range of potential uses enabled by these properties, such as sub-diffraction resolved imaging,[7] optical cloaking,[8] single-molecule biosensing,[9] and applications in nonlinear optics[10] and quantum optical circuits.[11]

One way of fabricating a type II HMM is via alternating nanoscale metal and dielectric layers. In addition to surface plasmon polaritons (SPPs) present on single metal layers, dielectric gaps between plasmonic metal layers support specific propagating or localized gap plasmon modes.[12] If such structures are extended to repeated multilayers, the landscape for plasmon polariton excitations will change due to coupling between adjacent gaps. Optically, several Bloch plasmon polariton (BPP) modes at different energies can be excited depending on the choice of metal and dielectric and the number of layers.[13,14] Alternatively, heavily doped

semiconductor layers can be used as substitutes for metals in realizing HMMs in the near-infrared.[15]

Like SPPs, BPPs can produce extremely confined and enhanced electromagnetic fields and therefore can be used for spectroscopic sensing with high sensitivity at specific nanoscale locations, for example with a bulk HMM film using a grating.[16] Nanoscale HMM structures can also have hyperbolic Bloch-like localized modes in addition to non-hyperbolic plasmonic modes and modes in the elliptical region of the material. In particular, antennas made of hyperbolic metamaterials can be used to control scattering and absorption of light over a broad spectral range, and their adjustable excitation peaks can be employed for hyperthermia in nanomedicine, fluorescence emission enhancement[17] and prospectively in photoacoustic imaging.[18] The opposite of such a system, a hole in a HMM, has corresponding gap plasmon modes due to Babinet's principle of complementarity.[19] Extending the hole to a slot provides a subwavelength scale waveguide useful for photonic nanocircuitry.[20] Similarly, metal wires and dielectric-filled tubes can be used as plasmonic waveguides.[21] Producing a multilayered system with a similar configuration results in a coaxial metal-dielectric-metal wire with the ability to use layer thicknesses to tune the effective refractive index for propagating waves.[22] Hyperbolic dispersion in deeply subwavelength structures sustains a wide series of surface and bulk modes. Unfortunately, only a very limited fraction of the supported modes can be excited by far field illumination, and often only by using adaptive optics (e.g. gratings[23] or prisms[24]) since this adds enough momentum to the incoming light to excite high-K modes.[25] However, when a grating is used, only the modes resulting from the overlap of grating modes and BPPs can be excited and probed. On the other hand, local excitation with a near-field optical probe or an electron beam can probe additional dark modes, since they probe the local plasmonic density of states.[26] Plasmonic dark modes have a zero net dipole moment, and thus cannot be excited with a plane wave that has a wavelength longer than the structure.[27]

Compared to bright modes with dipolar character, dark modes have narrower line widths and longer lifetimes, both due to the lack of a net dipole moment, which inhibits radiative losses.[28] The intrinsic difficulties in the direct optical excitation of these modes have hindered their measurement, understanding and exploitation.

A possible route for overcoming these limitations and acquiring a clear picture of the modes supported by a particular structure is to use electron energy loss spectroscopy (EELS). In fact, it allows to excite and map locally the distribution of electromagnetic modes by measuring the energy lost during the local interaction with the specimen. In EELS inside a scanning transmission electron microscope (STEM) a high-energy monochromatic electron beam (60-300 keV) passes through or near (aloof mode) the structure of interest, and the energy spectrum resulting from interactions is measured.[29] EELS can probe a wide range of excitations, including phonons at tens to hundreds of meV,[30] various plasmon types (localized, surface and bulk) as well as interband transitions in the eV range,[31] and the ionization edges of electron shells (10-1000 eV region). With new advances in monochromatic electron sources, the energy resolution of STEM-EELS can reach down to 10 meV whilst retaining sub-angstrom spatial resolution.[32-34] With this energy resolution, hyperbolic phonon-polaritons[35] and the surface and bulk vibrational modes of single nanoparticles[36] can be probed, and accurate measurements of surface plasmon peak widths can be used to study their kinetics.[37] When applied to plasmonics, an EELS spectrum corresponds to optical extinction, in contrast to a cathodoluminescence measurement, which probes optically radiative modes by measuring photons emitted due to interactions between the electron beam and the sample.[38,39] EELS is a useful tool for studying localized plasmon resonances of metal nanostructures,[40-42] and corresponding nanocavities.[26,43] By applying tomographic reconstruction techniques, mode excitations can be mapped in 3D.[44-47] In addition, plasmonic surface enhancements can be used to probe molecular excitations in

STEM-EELS.[48] EELS can also probe propagating plasmon polaritons,[49] including coupled SPP modes (or cavity modes) between thin metal layers.[50]

In this work we apply the latest generation of STEM-EELS to investigate the intrinsic optical properties of HMM nanostructures, namely without the need of a coupling device (grating coupling, for instance). The aim is to provide further and direct insights about surface and bulk plasmon polaritons in HMM nanostructures, so far only indirectly observed or excited. We characterize a number of structures with STEM-EELS, including films, pillars and holes of varying diameters as well as slots and coaxial resonators. Thus, we demonstrate experimentally both Bloch-like localized surface plasmon resonances and other plasmonic modes in HMM structures and propagating polaritons in extended slot and hemicylindrical coaxial waveguides, supported by simulations. HMM pillars support prominent geometry-dependent plasmon resonances,[17] and EELS measurements can provide direct evidence of their existence by using an independent excitation method that reveals both bright and dark modes in the system. The high energy resolution also enables the measurement of vibrational resonances in the HMM structures. Additionally, any possible plasmon polariton modes in the multilayer can be probed via the electron beam, removing the need of any additional coupling methods, which modifies the intrinsic resonances of the HMM structure.

2. Results

2.1. Sample Geometry

As sketched in **Figure 1**, we investigate different nanostructures such as pillars, holes, slots and coaxial structures. To produce a hyperbolic multilayer, a minimum of eight layers (four bilayers of metal and dielectric) is needed to achieve properties matching an anisotropic

effective medium prediction. However, the effective medium approach is more appropriate for large continuous features than complex nanostructures, so individual layers are used in our simulations. It should also be noted that there is both an elliptical and a hyperbolic dispersion region in metal-dielectric HMMs, in our multilayer the transition is at around 1.9 eV (650 nm wavelength), with hyperbolic dispersion at lower energies.[17,23] Adding bilayers to the system will increase the number of coupled plasmonic states, and the layers should be as thin as possible, taking into account the desired filling rate and the continuity of the metal film.[11] Thus, the HMM was designed to have ten alternating layers of gold (14 nm) and aluminum oxide (20 nm), as seen in Figure 1e, deposited on a standard transmission electron microscope (TEM) sample grid with an amorphous carbon film. The conformal atomic layer deposition (ALD) process for the dielectric produces an accumulated 100 nm dielectric layer on the other side of the carbon film, which shields the multilayer structure during focused ion beam (FIB) milling. This shield helps in making the slope of the edge more vertical for the rest of the structure. The extra layer does not have a significant effect on the EEL spectra.

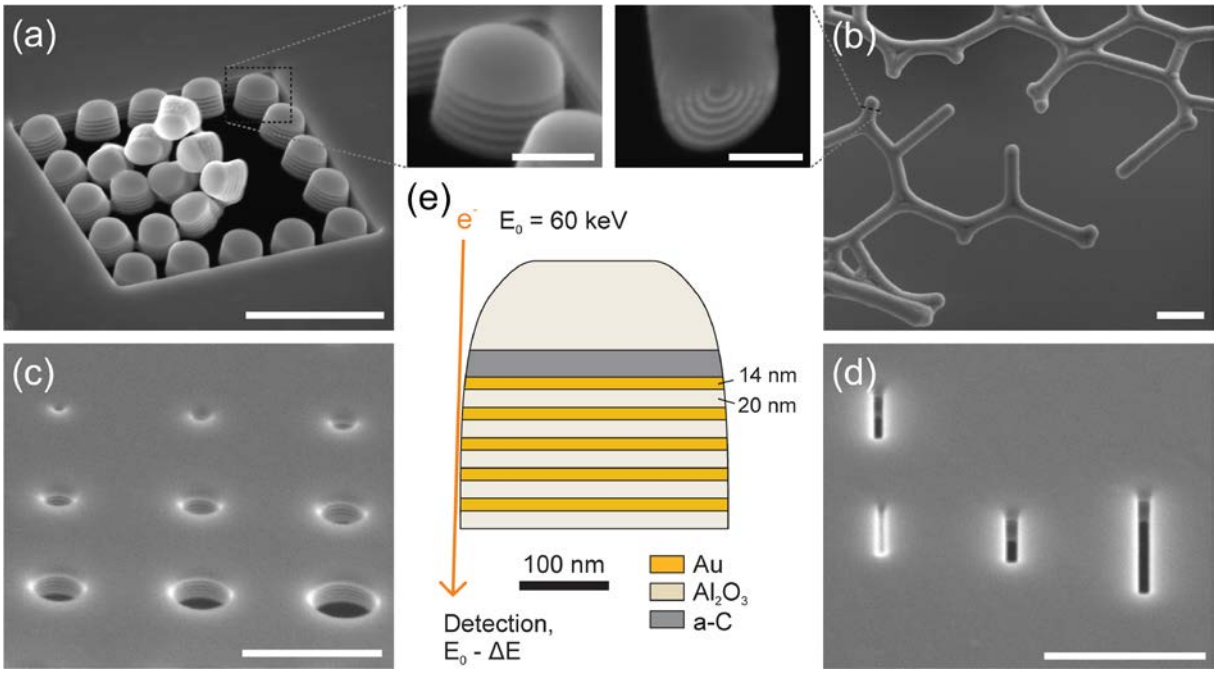

Figure 1. a-d) Scanning electron micrographs of structure types on the TEM grid measured with EELS, imaging angle 52° from normal. a) An array of HMM pillars, diameters 300 nm, with a magnified inset of a single pillar. b) coaxial HMM waveguides deposited on carbon filaments with an inset of a milled cross section of a similar filament. c) Holes in the HMM film ranging from 50 to 450 nm in diameter with steps of 50 nm, and d) slots of 500 nm and 1 µm length in the HMM. Horizontal scale bars 1 µm in main images and 200 nm in insets. e) A schematic of an EELS measurement with a cross section of a 300 nm diameter HMM pillar. All structures considered in this paper have the same layers and similar edge profiles, with a typical deviation from vertical of 20 nm between top and bottom metal layers.

2.2. EELS Results

EEL spectra of HMM pillars with different radii are shown in **Figure 2**. The low-energy excitation spectrum of the edge of the HMM film has the broad surface plasmon peak of the thin polycrystalline gold film as its main consistent feature near 2.3 eV (marked "Au SP").[51] In the EEL spectra, HMM pillars display a series of loss peaks, which are clearest when the beam grazes the edges of all the metal layers in the HMM. Since the pillars are slightly cone-like and tilted, the relative intensities of the peaks vary around the pillars. For pillars with diameters of 300 nm, 450 nm and 600 nm the resonances shift to lower energies with increasing pillar sizes: the most intense peaks are marked with 1 at 980 meV, 670 meV and 520 meV respectively in Figure 2d, peak fits are shown in **Table S1**. A set of higher order modes (marked 2-4 for each pillar) are clearly visible. Additional low-energy resonances (marked "p") are experimentally detected, with the most intense peaks at 370 meV (300 nm), 260 meV (450 nm) and 200 meV (600 nm diameter), which are likely localized surface phonon resonances not accounted for in the corresponding simulations.[52] There is a weakly visible additional peak at 350 meV in spectra measured close to HMM edges in general that

does not depend on the structure, possibly a vibrational signal originating from the amorphous carbon support, with intensity dependent on the proximity of exposed carbon.[53] At higher energy, there is a wide peak near 25 eV (**Figure S1**). This corresponds to the bulk plasmon peaks of both gold and aluminum oxide, which are only visible in transmission through the layers.

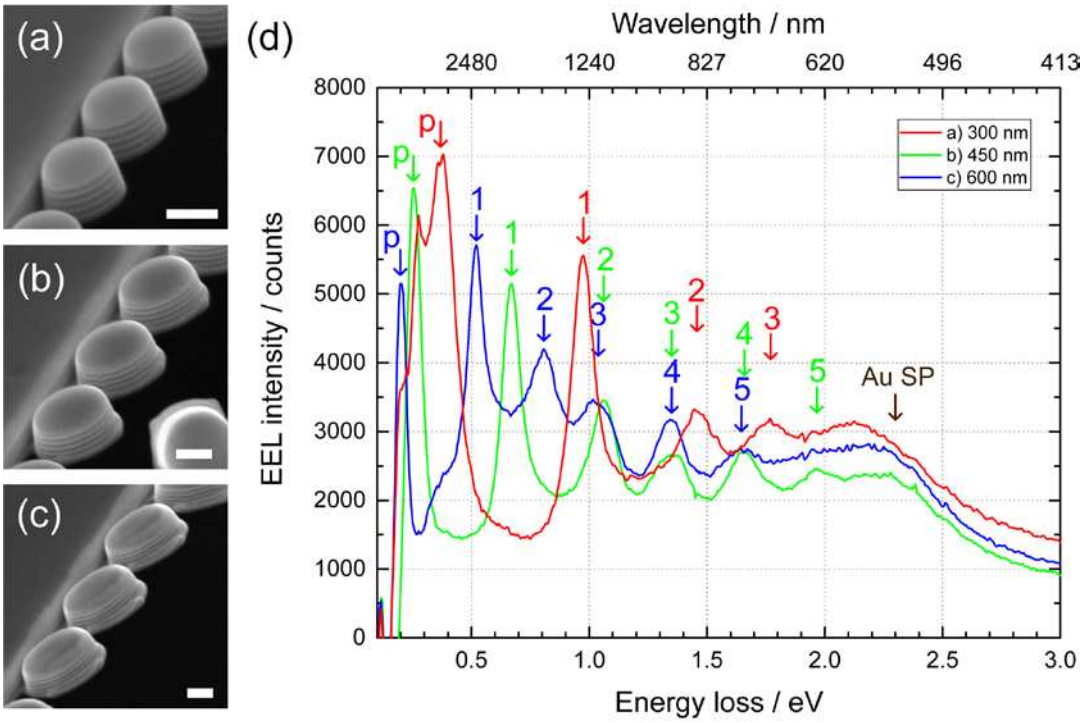

Figure 2. a-c) SEM images of FIB-milled HMM pillars attached to the main film on the left side imaged with a 52° tilt, diameters a) 300 nm, b) 450 nm and c) 600 nm. Scale bars 200 nm. d) Experimental EEL spectra with the zero-loss peak subtracted and principal component analysis applied for HMM pillars of 3 different diameters (in a-c) with the beam grazing the edge. Plasmonic modes are highlighted with numbers 1-5 for each pillar size and the geometry-dependent low-energy mode is marked "p".

To confirm whether the resonances are modified when the orientation of the pillar changes, we also changed the orientation of the pillar in respect to the incident beam. When the beam

grazes the bottom layer of the pillar (with dielectric), the SP peak is lower but the plasmonic peaks associated with the dipole and quadrupole (1 and 2 in Figure 2d) remain at the same positions as for the simulation where the beam grazes the edges of the metal layers. The positions of the peaks are unchanged in the experiments, where a tilted pillar in the array was compared to an upright one (**Figure 3**). For the roughly horizontal beam in relation to the measured pillar in the experiment, there is an additional, possibly phononic, peak at 0.35 eV, and high order plasmonic peaks are poorly visible. For similar pillars, the location of the optical absorption peak (electric dipole resonance) has been shown to be independent of the orientation of the pillar.[17]

The low-energy geometry-dependent resonance (phonon) is clearly shifted to higher energies with additional physical connections to the bulk, as seen for the corner pillars in Figure 3a and **S2a**. In these cases, plasmonic resonances are almost unaffected by the additional coupling.

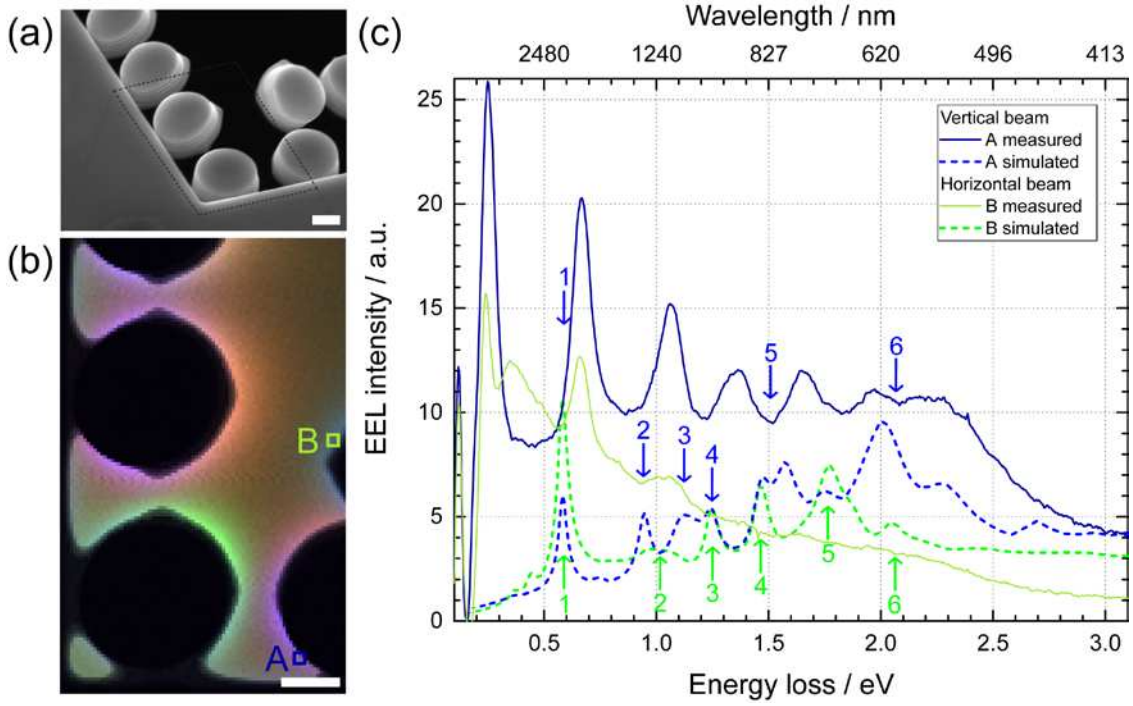

Figure 3. HMM pillars with a diameter of 450 nm, orientation dependence. a) SEM image with a 52° tilt, EELS area highlighted. b) EELS map measured perpendicular to the substrate with color channels red 0.27 eV, green 0.39 eV and blue 0.68 eV, channel width 0.01 eV. Scale bars 200 nm. c) Experimental (PCA applied) and simulated EELS spectra of the HMM pillars with different beam directions. The vertical beam is perpendicular to the plane of the layers, while the horizontal beam grazes the bottom of the pillar. Numbered arrows refer to energies of near-field simulations in Figure 4.

2.3. Simulation Results

To interpret the specifics of the modes in the pillars, we simulated the energy loss experienced by the electrons with the finite element method. For the spectra of the pillar in Figure 3b, there is a good agreement with the experiment in the case of the vertical beam, as peaks 3 and 4 can be interpreted as double peaks in the experiments due to their wide linewidths. The simulations show a more complicated spectrum, and the effect of the coupling between metal layers seems to be more pronounced in the ideal structure than in the experiments.

The specifics of the modes excited by the electron beam are shown by the simulated near-field distributions **(Figure 4a).** For the vertical beam grazing the 450 nm HMM pillar, the most prominent peaks in simulation are the dipole at 0.58 eV (peak 1 in the figure), the quadrupole at 0.95 eV (2) and the hexapole at 1.24 eV (4). For the horizontal beam, near-field intensities are also mainly similar, as shown in Figure 4b. There are more complicated resonances visible in the simulations (3, 5 and 6) that are possibly created due to coupling of plasmonic excitations between metal layers, and not visible in the experiments due to defects in the multilayer structure.

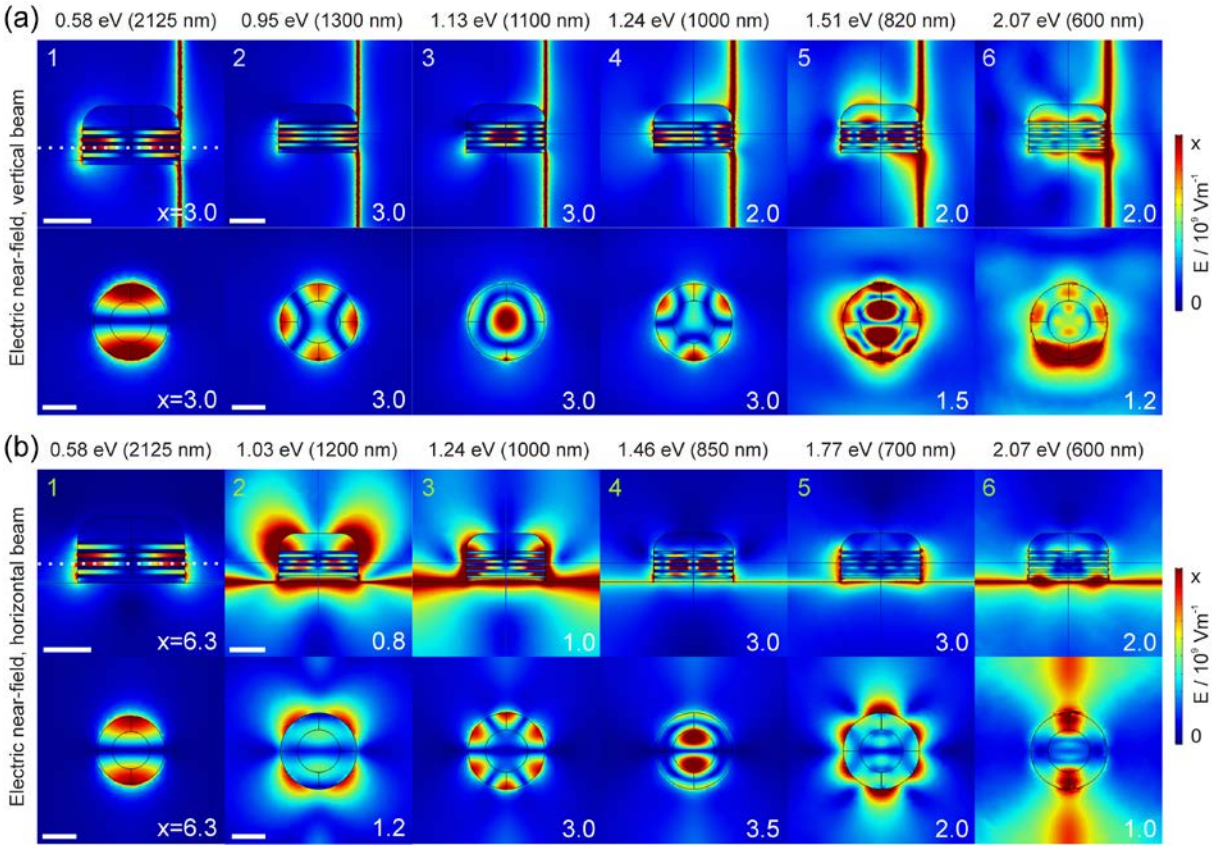

Figure 4. Simulated near-field intensity maps of the electric fields of a 450 nm diameter pillar when using a) vertical and b) horizontal current at different energy losses. Cross sections parallel to pillar axis shown on top, aligned to the beam and pillar center. In the lower rows, the plotted horizontal cross section is along the third Al_2O_3 layer from the bottom, marked with a white dotted line in the top left plot. The maximum value of the color scale is marked at lower right in each plot. The simulated resonances are marked in Figure 3, and the corresponding simulated magnetic field plots are in Figure S3. Scale bars 200 nm.

To study the correspondence between optical absorption peaks seen in similar structures[17] with the EELS peak, we simulated absorption and scattering spectra using a plane wave and the corresponding near-field intensities for the HMM pillars. The results are shown in **Figure 5**. The additional excitations seen in the EEL spectra compared to extinction spectra are a bright example of the limits of investigating these modes by using conventional approaches.

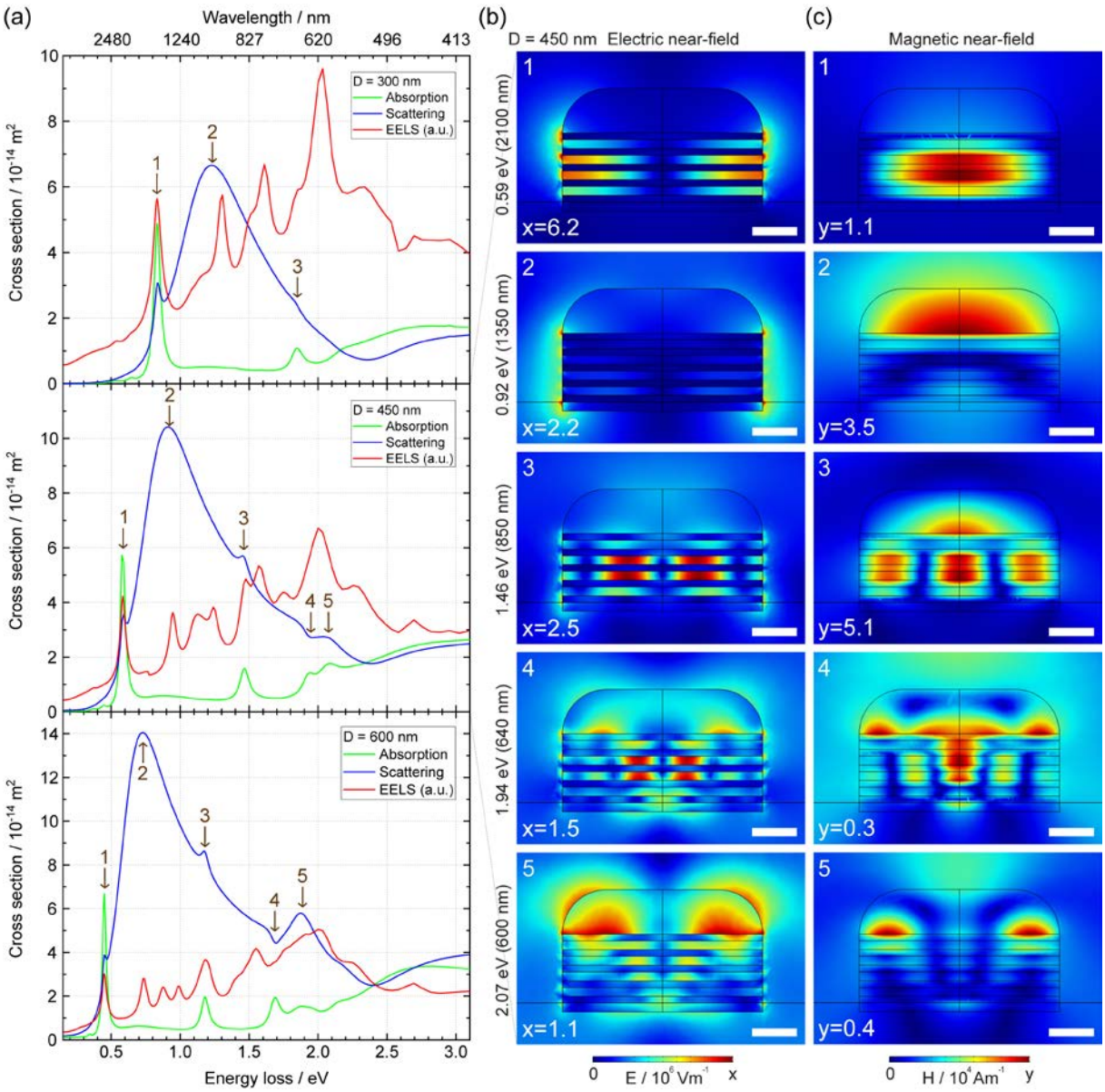

Figure 5. a) Simulated optical absorption and scattering spectra of HMM pillars with three different diameters compared with EELS simulations using a vertical beam. Absorption and scattering cross sections are comparable between each other and between pillar sizes, while the EEL spectra are comparable only between pillar sizes, using arbitrary units. b) Electric and c) magnetic near-field intensities in the 450 nm pillar using plane wave excitation with marked energies. The plane wave propagates from the top, along the axis of symmetry of the pillar. The corresponding resonances are marked with numbered arrows in a), and resonances

with similar field profiles for other pillar diameters are marked with the same number. The maximum value of the color scale is marked at lower right in each plot. Scale bars 100 nm.

The most prominent modes are similar to the ones seen on single plasmonic nanodisks. Evaluating the modes as they would be on a single disk, the optical absorption spectra show clearly that a dipole-like mode (1 in Figure 5) is the main bright mode, and hexapole (3) and decapole modes (split to 4 and 5) are also clearly visible. These modes have a non-zero dipole moment, while the quadrupole and octupole are dark due to them being symmetric for the purposes of plane wave excitation. Additional peaks seen in the EELS simulations are not prominent in the optical spectra, and the main scattering mode (2) does not have a corresponding peak visible in the experimental EELS spectrum, but simulated EELS spectra have similar features, as seen most prominently in mode 2 in Figure 4b.

2.4. Other HMM Structures

In view of Babinet's principle,[54] we measured also the opposite of the pillar system, i.e., holes in the HMM. EELS measurements of the holes milled in the continuous HMM film did not reveal prominent size-dependent resonances as seen in **Figure S5**, as the SP is by far the dominant plasmonic excitation in all holes. As an analogue, single nanoholes in silver have dipole and quadrupole resonances.[43] However, in our simulations of holes in the HMM the resonances are relatively weak, and in the experiments any visibility is further limited because the beam does not optimally graze all the edges as with the pillars.

Extending a hole in the HMM to a slot produces a structure that is useful as a plasmonic waveguide. Gap plasmon polaritons have an extraordinary mode confinement and an appreciable propagation length.[26] Measurements of these slot resonators display standing

waves, which can be excited most effectively at resonant positions on the edge of the HMM. For a 1000 nm by 70 nm slot the mode with two nodes and one maximum is experimentally at 430 meV, the mode with two maxima at approximately twice the energy, and continuing with the same pattern, experimentally recognizable to up to five maxima **(Figure 6)**. The standing wave patterns fit well to sine function profiles. The peaks are clear in the spectra at resonant locations, and simulated spectra agree well with the measurements (Figure 6b,c). For a shorter slot with a length of approximately 500 nm, the resonances with the same number of maxima are almost twice the energy of the longer slot **(Figure S4)**.

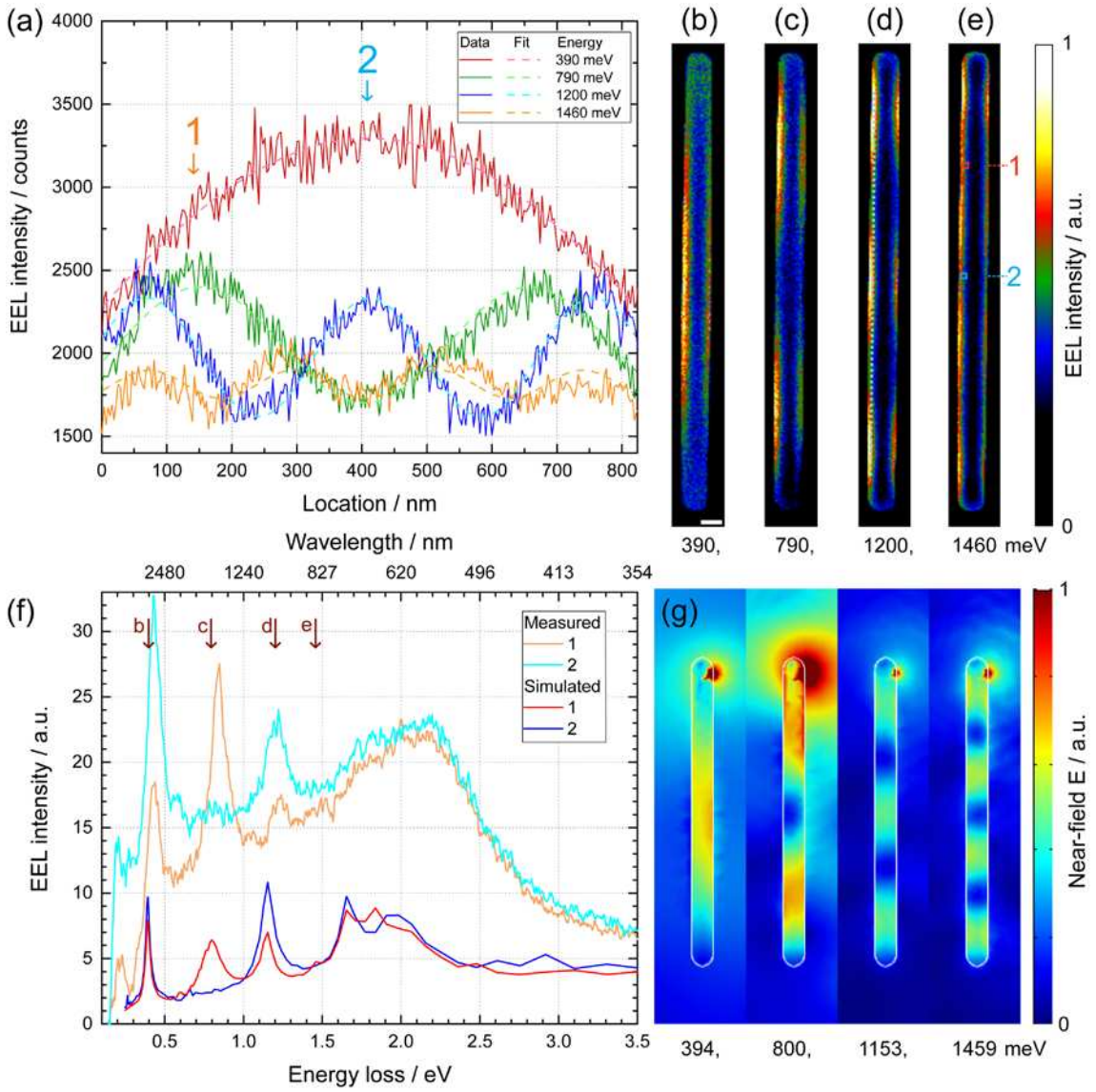

Figure 6. HMM slot resonator, length 1000 nm, width 70 nm. a) EELS profiles at specified energies (10 meV energy channel width) on the marked line on the edge of the slot from top

to bottom in d) using raw data. Sine function fits applied to profiles. b-e) Experimental EELS intensity maps of the slot at marked energy losses. Scale bar 50 nm. f) Simulated and experimental EELS spectra at two positions marked in e) with resonant peaks marked and the zero-loss peak substracted. g) Simulated electric field intensities of the same slot at specified energies. Electron beam applied to a single spot at top right in each case.

Finally, we measured rod-like HMM structures, or coaxial waveguides (see Figure 1b). Their fabrication was possible due to thin carbon filaments originally present on the holey carbon film of the TEM grid. Since the gold layers were sputtered (deposition occurring more isotropically than with e-beam evaporation), hemicylindrical coaxial HMM resonators **(Figure S6)** with a diameter of about 350 nm were created without the need of any FIB milling. These resonators have only low-energy resonances visible, since the dielectric covers the entire outer surface (Figure S6b). Due to this, phononic resonances are prominently visible, while plasmonic ones are difficult to probe. A FIB-milled version of the filament displays additional resonances visible at 1-2 eV including the SP, due to exposed metal surfaces **(Figure S7)**.

3. Discussion

Plasmon excitations measured on a straight HMM edge without additional features are dominated by the SP at 2.3 eV. Any modes associated with the whole HMM structure do not form distinct peaks, but fill the energy range below the SP peak. As on porous gold, there can be localized plasmon resonances on rough gold surfaces that are dependent on the local topography, but the SP peak dominates when averaging over a large area.[53] In our case, FIB-

milled surfaces were smooth enough to lack spatially separated localized resonances. The metal layers were also sufficiently thick to be continuous.

The measured HMM pillars show a clear set of resonances at low energies that involve the whole pillar based on near-field simulations, and the simulated EEL spectra generally match the experiments except for a consistent redshift in the simulated peak locations, which can be due to different effective refractive indices in the actual samples due to imperfections in the structures. The dipole mode is the strongest of the plasmonic modes, which is a localized hyperbolic Bloch-like plasmon as shown by simulations with similar HMM pillars in [17], and as a bright mode it is also visible as an absorption peak in optical spectra. For each pillar diameter, there are modes at higher energies that are also clear in the EELS spectra up to the SP peak. However, these higher order modes are observed in the elliptical region, and in addition to a HMM[55] can also be supported by a simpler multilayer, such as a metal-dielectric-metal system.[56] As expected, the energies of the localized plasmon modes decrease for increasing pillar diameter. The near-field simulations show a set of dipolar, quadrupolar and hexapolar modes that are similar to the resonances seen in metal nanodisks.[57] Simulations of energy loss spectra for different pillar sizes (**Figure S8**) show a similar general pattern, with different energies for each size. The magnetic contribution for the energy loss is 3 orders of magnitude lower than the electric for all the resonances, so none of them have a distinctly magnetic character. Additionally, near-field simulations reveal more complicated modes, that possibly arise from coupling between disks in the stack. There is also a clear low-energy mode at 200-400 meV that is size-dependent as well (Figure 2d). This points to a localized confined surface phonon mode, the phononic equivalent to a LSPR.[52] In this case, the aluminum oxide discs in the structures are possibly the main contributors to these resonances, as dielectric nanoparticles display phononic modes at similar energies in EELS measurements.[36] Coupling of modes between pillars adjacent to each other is relevant only

for the phononic modes, as the plasmonic ones are not seen when the beam is in the ~100 nm wide gap between the pillars.

Peaks visible in simulated optical absorption spectra for the HMM pillars correlate well with the simulated EELS spectra, and allow the assignment of bright and dark modes. The main scattering peak does not feature prominently in the EELS spectra, at least not at exactly the same energies in simulations, and it is undetectable in EELS measurements.

In straight slots milled into the HMM the standing wave patterns are in good agreement with the simulations, except for the slight general redshift in peak energies, and they can be interpreted as interference due to counter-propagating gap plasmons.[26] These gap plasmon resonators are analogous to ones on single metal layers showing similar patterns, [54] and as such the modes are not hyperbolic in nature. The propagating modes illustrate that HMM gaps can be used as plasmonic waveguides with a high field confinement.

4. Conclusion

Nanostructures with hyperbolic dispersion have useful features, such as the separate adjustability of optical absorption and scattering with geometry in pillars, that can be employed in numerous applications. EELS measurements of them reveal clear resonances of both plasmonic and likely phononic modes dependent on the geometry of the features, including higher order dark modes. Their origin in many cases is not hyperbolic though, and needs measures such as nanoimaging of polarized wave fronts or simulations to prove. HMM pillar resonators in particular displayed clear plasmonic resonances that involved the entire structure, with coupling between different metal layers across several dielectric gaps. Simulated EELS spectra support the identification of the resonances as plasmonic modes, and

plane wave simulations provided insight on the optical nature of the modes. Cavities milled in HMM can be applied as subwavelength waveguides, and they showed clear evidence of propagating gap plasmons supported by the HMM with standing wave patterns dependent on the length of the slots. Using STEM-EELS, a sub-nanometer spatial and a meV-scale energy resolution for the coupling of electric fields to the HMM structures was achieved, which provides a better understanding of the plasmonic and phononic modes and their localization in the nanoscale.

5. Experimental Section

Sample Fabrication: The hyperbolic metamaterial sample consisted of repeated layers of metal and dielectric produced on a TEM Cu grid covered with a holey carbon film (HC200-CU, Electron Microscopy Sciences, 200 mesh, 50 µm thick). The carbon film in continuous areas away from the original hole edges was measured to be (29±5) nm with EELS in transmission. Sputtering at room temperature (Kenosistec KS500C) was used to produce the first gold layer with a thickness of 14 nm as measured by ellipsometry and atomic force microscopy. On top of this, 20 nm of aluminum oxide, confirmed with ellipsometry, was produced with an ALD process using trimethylaluminum and oxygen plasma as precursors at 80 °C in an Oxford Instruments FlexAL reactor. These two deposition processes were repeated five times to produce an alternating multilayer on the carbon film. As a result of the ALD process, Al_2O_3 was also deposited on the other side of the carbon film (approximately 100 nm, Figure 1e). Patterns on the multilayer were produced by FIB milling with a 30 kV gallium ion beam using a FEI Helios NanoLab 650 dual beam system. The milling was done at 7.7 pA current from the side of the thick Al_2O_3 film, which acted as a protective layer for the main HMM structure. Scanning electron micrographs were taken after milling to characterize the structures.

EELS Measurements: STEM EELS was performed using a monochromated Nion Ultra-STEM 100MC Hermes at the SuperSTEM facility in Daresbury, UK. The sample was loaded into vacuum on the previous day, after a bake at 120 °C (in vacuum) prior to the measurements to prevent contamination during scanning. During the measurements, the sample was perpendicular to the beam and the measurement was done from the side of the copper supports of the TEM grid, so that the thick Al_2O_3 layer was on the side facing the incoming beam. The acceleration voltage was 60 kV, the probe convergence semiangle (i.e. of the excitation) was 31 mrad and the EELS collection semi-angle was 44 mrad. The zero-loss peak (ZLP) full width at half maximum (FWHM) was adjusted to between 25 and 30 meV for low-loss EELS spectra collected for this article (Figure S2c), as a compromise between optimal energy resolution and beam current (approx. 11-15 pA) for signal-to-noise. Both low-loss spectra with the ZLP positioned on the detector as well as high-loss spectra with higher integration time and the ZLP shifted just off the detector were acquired simultaneously to form spatially resolved spectrum images with a typical acquisition time of 0.16 s/pixel and pixel sizes between 2 and 15 nm depending on the image. The dispersion used was 5 meV/channel with a measured energy range of 0-10 eV for all data except Figure S1. High angle annular dark field (HAADF) images were acquired before the EELS scan (and compared to check for any sign of damage to the structure of for signs of adventitious carbon contamination). All of the structures were prepared on the same TEM membrane, and the measurements were done without removing the sample from the vacuum chamber between them.

Data Analysis: Energy correction was first done for both all low- and high-loss spectra based on the ZLP visible in the low-loss spectrum. Plasmon peaks visible on both spectra were used for a further correction of the high-loss spectrum (85 meV added to raw energy values with 5 meV dispersion, 340 meV with 20 meV dispersion). A first order log-polynomial background with a fit on the approximate range of 110 meV to 140 meV was used separately for each

spectrum to remove the ZLP from the spectra, except where noted otherwise. The data was processed using Gatan Digital Micrograph v3.30. For EELS spectra, corresponding photon wavelengths are used in graphs as an additional axis for comparison purposes, but photons were not detected in the measurements. Hyperspectral image maps were plotted with signal intensity linearly related to color intensity in three individual channels (arbitrary units) and merged to RGB images. All energy values of loss peak positions have been rounded to the nearest 10 meV, and their uncertainty is estimated to be ±20 meV. Where noted, principal component analysis (PCA)[58] with varying numbers of components (25-38 depending on the image) was used to smooth the hyperspectral EELS image maps or spectra, after careful inspection of the signal residuals and individual components to avoid introducing processing artefacts or discarding significant information. Peak locations and linewidths as seen in Table S1 were determined with gaussian function fits using OriginPro 2016.

Simulation details: Numerical results were obtained using the finite element method implemented in the RF Module in COMSOL Multiphysics, version 5.3. In the calculations, we model a single structure following de Abajo,[59] applying scattering boundary conditions to the vertical sides of the cell. The electron beam, moving in the z direction, is modelled as a line current $j_z(\boldsymbol{R},\omega) = ev\delta(\boldsymbol{R}-\boldsymbol{R}_0)e^{ik_e z}$, where δ is the Dirac delta function and R = (x,y) with $R_0 = (x_0,y_0)$ being the transverse location of the electron beam. Here, *e* is the charge of the electron, $v = 0.446c$ is the electron speed corresponding to an acceleration voltage of 60 keV, c is the speed of light in vacuum, and ke = ω/v. The permittivity of gold is taken from Rakic,[60] whereas the refractive index of Al_2O_3 assumes the constant value 1.75 in the considered energy range. Simulations of optical scattering, absorption, and extinction cross sections of single, isolated HMM pillars were performed in a similar manner with the same software, but by using a linearly polarized plane wave as in [17] instead of a line current. The scattering cross-section is defined as $\sigma_{scat} = \frac{1}{I_0}\iint(\boldsymbol{n}\cdot\boldsymbol{S})\,dS$, where I_0 is the intensity of the

incident light, $\boldsymbol{n}$ is the normal vector pointing outward from the structure and S is the Poynting vector. The integral is taken over the closed surface of the pillar. The absorption cross section equals $\sigma_{abs} = \frac{1}{I_0} \iiint Q dV$, where Q is the power loss density of the system and the integral is taken over the volume of the structure.

Supporting Information

Supporting Information is available from the Wiley Online Library or from the author.

Acknowledgements

SuperSTEM is the UK National Facility for Advanced Electron Microscopy, supported by the Engineering and Physical Sciences Research Council (EPSRC). NM acknowledges the financial support from the FEDER program (grant n. 2017-03-022-19 Lux-Ultra-Fast) and the Luxembourg National Research Fund (CORE Grant No. C19/MS/13624497 'ULTRON'). The authors thank Dr. Rosaria Brescia for preliminary EELS measurements and valuable discussions.

References

[1] P. Shekhar, J. Atkinson, Z. Jacob, *Nano Converg.* **2014**, *1*, 14.

[2] A. Poddubny, I. Iorsh, P. Belov, Y. Kivshar, *Nat. Photonics* **2013**, *7*, 948.

[3] C. T. Riley, J. S. Smalley, J. R. Brodie, Y. Fainman, D. J. Sirbuly, Z. Liu, *Proc. Natl. Acad. Sci. USA* **2017**, *114*, 1264.

[4] K. V. Sreekanth, M. ElKabbash, Y. Alapan, A. R. Rashed, U. A. Gurkan, G. Strangi, *Sci. Rep.* **2016**, *6*, 26272.

[5] T. Xu, A. Agrawal, M. Abashin, K. J. Chau, H. J. Lezec, *Nature* **2013**, *497*, 470.

[6] V. Caligiuri, L. Pezzi, A. Veltri, A. De Luca, *ACS Nano* **2017** *11*, 1012.

[7] Z. Liu, H. Lee, Y. Xiong, C. Sun, X. Zhang, *Science* **2007**, *315*, 1686.

[8] W. Cai, U. K. Chettiar, A. V. Kildishev, V. M. Shalaev, *Nat. Photonics* **2007**, *1*, 224.

[9] A. Kabashin, P. Evans, S. Pastkovsky, W. Hendren, G. Wurtz, R. Atkinson, R. Pollard, V. Podolskiy, A. Zayats, *Nat. Mater.* **2009**, *8*, 867.

[10] B. Wells, Z. Kudyshev, N. Litchinitser, V. Podolskiy, *ACS Photonics* **2017**, *10*, 2470-2478.

[11] C. Cortes, W. Newman, S. Molesky, Z. Jacob, *J. Opt.* **2012**, *14*, 063001.

[12] A. F. Koenderink, A. Alù, A. Polman, *Science* **2015**, *348*, 516.

[13] I. Avrutsky, I. Salakhutdinov, J. Elser, V. Podolskiy, *Phys. Rev. B* **2007**, *75*, 241402.

[14] T. Li, J. B. Khurgin, *Optica* **2016**, *3*, 1388.

[15] G. V. Naik, A. Boltasseva, *Metamaterials* **2011**, *5*, 1.

[16] Y. Lee, S.-J. Kim, H. Park, B. Lee, *Sensors* **2017**, *17*, 1726.

[17] N. Maccaferri, Y. Zhao, T. Isoniemi, M. Iarossi, A. Parracino, G. Strangi, F. De Angelis, *Nano Lett.* **2019**, *19*, 1851.

[18] Y.-S. Chen, Y. Zhao, S. J. Yoon, S. S. Gambhir, S. Emelianov, *Nat. Nanotechnol.* **2019**, 14, 465.

[19] M. Horák, V. Křápek, M. Hrtoň, A. Konečná, F. Ligmajer, M. Stöger-Pollach, T. Šamořil, A. Paták, Z. Édes, O. Metelka, J. Babocký, *Sci. Rep.* **2019**, *9*, 4004.

[20] H. Choo, M.-K. Kim, M. Staffaroni, T. J. Seok, J. Bokor, S. Cabrini, P. J. Schuck, M. C. Wu, E. Yablonovitch, *Nat. Photonics* **2012**, *6*, 838.

[21] F. I. Baida, A. Belkhir, D. Van Labeke, O. Lamrous, *Phys. Rev. B* **2006**, *74*, 205419.

[22] R. de Waele, S. P. Burgos, H. A. Atwater, A. Polman, *Opt. Express* **2010**, *18*, 12770.

[23] K. V. Sreekanth, A. De Luca, G. Strangi, *Sci. Rep.* **2013**, *3*, 3291.

[24] L. Luo, T. Tang, *Superlattice Microst.* **2016**, *94*, 85.

[25] K. V. Sreekanth, A. De Luca, G. Strangi, *J. Opt.* **2014**, *16*, 105103.

[26] S. Raza, M. Esfandyarpour, A. L. Koh, N. A. Mortensen, M. L. Brongersma, S. I. Bozhevolnyi, *Nat. Commun.* **2016**, *7*, 13790.

[27] N. C. Lindquist, P. Nagpal, K. M. McPeak, D. J. Norris, S.-H. Oh, *Rep. Prog. Phys.* **2012**, *75*, 036501.

[28] D. Gómez, Z. Teo, M. Altissimo, T. Davis, S. Earl, A. Roberts, Nano Lett. **2013**, *13*, 3722.

[29] O. L. Krivanek, T. C. Lovejoy, N. Dellby, T. Aoki, R. W. Carpenter, P. Rez, E. Soignard, J. Zhu, P. E. Batson, M. J. Lagos, R. F. Egerton, P. A. Crozier, *Nature* **2014**, *514*, 209.

[30] R. F. Egerton, *Ultramicroscopy* **2015**, *159*, 95.

[31] P. Z. El-Khoury, P. Abellan, Y. Gong, F. S. Hage, J. Cottom, A. G. Joly, R. Brydson, Q. M. Ramasse, W. P. Hess, *Analyst* **2016**, *141*, 3562.

[32] E. P. Bellido, D. Rossouw, G. A. Botton, *Microsc. Microanal.* **2014**, *20*, 767.

[33] F. Hage, D. Kepaptsoglou, Q. Ramasse, L. Allen, *Phys. Rev. Lett.* **2019**, *122*, 016103.

[34] R. F. Egerton, *Rep. Prog. Phys.* **2008**, *72*, 016502.

[35] A. A. Govyadinov, A. Konečná, A. Chuvilin, S. Vélez, I. Dolado, A. Y. Nikitin, S. Lopatin, F. Casanova, L. E. Hueso, J. Aizpurua, *Nat. Commun.* **2017**, *8*, 95.

[36] M. J. Lagos, A. Trügler, U. Hohenester, P. E. Batson, *Nature* **2017**, *543*, 529.

[37] M. Bosman, E. Ye, S. F. Tan, C. A. Nijhuis, J. K. Yang, R. Marty, A. Mlayah, A. Arbouet, C. Girard, M.-Y. Han, *Sci. Rep.* **2013**, *3*, 1312.

[38] A. Losquin, M. Kociak, *ACS Photonics* **2015**, *2*, 1619.

[39] E. J. R. Vesseur, R. Waele, M. Kuttge, A. Polman, *Nano Lett.* **2007**, *7*, 2843.

[40] F. Song, T. Wang, X. Wang, C. Xu, L. He, J. Wan, C. Van Haesendonck, S. P. Ringer, M. Han, Z. Liu, G. Wang, *Small* **2010**, *6*, 446.

[41] Y. Wu, G. Li, C. Cherqui, N. W. Bigelow, N. Thakkar, D. J. Masiello, J. P. Camden, P. D. Rack, *ACS Photonics* **2016**, *3*, 130.

[42] D. T. Schoen, A. C. Atre, A. García-Etxarri, J. A. Dionne, M. L. Brongersma, *Nano Lett.* **2014**, *15*, 120.

[43] W. Sigle, J. Nelayah, C. T. Koch, P. A. van Aken, *Opt. Lett.* **2009**, *34*, 2150.

[44] A. Hörl, G. Haberfehlner, A. Trügler, F.-P. Schmidt, U. Hohenester, G. Kothleitner, *Nat. Commun.* **2017**, *8*, 37.

[45] O. Nicoletti, F. La Peña, R. K. Leary, D. J. Holland, C. Ducati, P. A. Midgley, *Nature* **2013**, *502*, 80.

[46] S. M. Collins, E. Ringe, M. Duchamp, Z. Saghi, R. E. Dunin-Borkowski, P. A. Midgley, *ACS Photonics* **2015**, *2*, 1628.

[47] G. Haberfehlner, F.-P. Schmidt, G. Schaffernak, A. Hörl, A. Trügler, A. Hohenau, F. Hofer, J. R. Krenn, U. Hohenester, G. Kothleitner, *Nano Lett.* **2017**, *17*, 6773.

[48] A. Konečná, T. Neuman, J. Aizpurua, R. Hillenbrand, *ACS Nano* **2018**, *12*, 4775.

[49] D. Rossouw, G. A. Botton, *Phys. Rev. Lett.* **2013**, *110*, 066801.

[50] H. Saito, K. Namura, M. Suzuki, H. Kurata, *Microscopy* **2013**, *63*, 85.

[51] W. Grogger, F. Hofer, G. Kothleitner, B. Schaffer, *Top. Catal.* **2008**, *50*, 200.

[52] H. Lourenço-Martins, M. Kociak, *Phys. Rev. X* **2017**, *7*, 041059.

[53] P. Abellan, P. Z. El-Khoury, Q. M. Ramasse, *Microscopy* **2017**, *67*, i30.

[54] B. Ögüt, R. Vogelgesang, W. Sigle, N. Talebi, C. T. Koch, P. A. van Aken, *ACS Nano* **2011**, *5*, 6701.

[55] X. Yang, J. Yao, J. Rho, X. Yin, X. Zhang, Nature Photon. **2012**, *6*, 450.

[56] G. Schaffernak, M.K. Krug, M. Belitsch, M. Gašparić, H. Ditlbacher, U. Hohenester, J. R. Krenn, A. Hohenau, *ACS Photonics* **2018**, *5*, 4823.

[57] F. P. Schmidt, H. Ditlbacher, F. Hofer, J. R. Krenn, U. Hohenester, *Nano Lett.* **2014**, *14*, 4810.

[58] M. Bosman, M. Watanabe, D. Alexander, V. Keast, *Ultramicroscopy* **2006**, *106*, 1024.

[59] F. J. G. de Abajo, *Rev. Mod. Phys.* **2010**, *82*, 209.

[60] A. Rakić, A. Djurišic, J. Elazar, M. Majewski, *Appl. Opt.* **1998**, *37*, 5271.

Hyperbolic metamaterial structures are studied with a local electron probe, revealing bright and dark plasmonic modes and phononic excitations. Energy loss close to multilayered metal/dielectric pillars reveals dipole, quadrupole and higher order localized modes, identified with simulations, with coupling across the dielectric gaps. Propagating gap plasmons are detected as interference patterns in metamaterial slot waveguides.

Plasmonic Nanostructures

T. Isoniemi, N. Maccaferri, Q. M. Ramasse, G. Strangi, F. De Angelis*

Electron Energy Loss Spectroscopy of Bright and Dark Modes in Hyperbolic Metamaterial Nanostructures

ToC figure: 55 mm × 50 mm